SUPPLEMENTARY INFORMATION

Precursor Design for Additive Manufacturing of Ceramics through Hydrogel Infusion

Natalie S. Yaw[1,2], Maryline G. Ferrier[1], R. Joey Griffiths[1], Joshua A. Hammons[1], Andrew J. Swift[1], Silvina A. Di Pietro[1], Jean-Baptiste Forien[1], Bradley C. Childs[1], Aiden A. Martin*[1], Kiel S. Holliday[1], Xiaofeng Guo[2], Jason R. Jeffries[1]*

[1] Physical and Life Sciences Directorate, Lawrence Livermore National Laboratory, 7000 East Avenue, Livermore, CA 94550, United States

[2] Department of Chemistry, Washington State University, Pullman, WA 99163, United States.

* Corresponding author e-mail: kerlin4@llnl.gov; martin248@llnl.gov

Supplementary Information table of contents:

Supplementary Figures

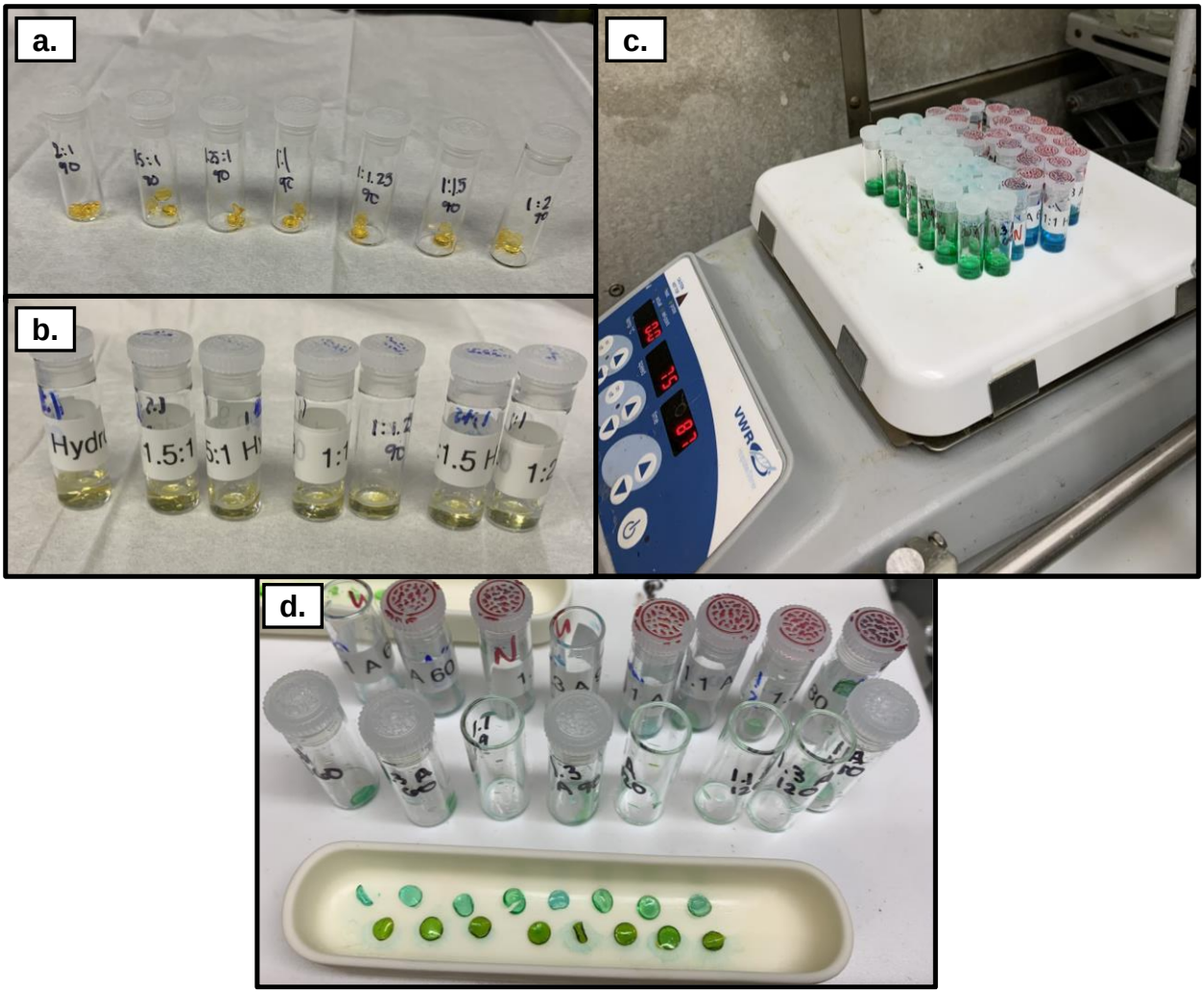

Figure S1. images of hydrogel discs throughout the curing, washing, and infiltration process. (a) Freshly cured organogel disks are a clear yellow (b) after washing and solvent swapping to water, hydrogels are translucent and pale yellow. (c) Hydrogel soaking in metal salt solutions (blue for copper nitrate and green for copper chloride), and (d) upon infusion hydrogels adopt the blue (top row in crucible) and green (bottom row in crucible) hues of the salt solutions.

Note: the hydrogel infused with copper nitrate have a blue-green tint since the starting color of the hydrogel was yellow and the copper nitrate solution was blue, leading to a final blue-green hydrogel disc.

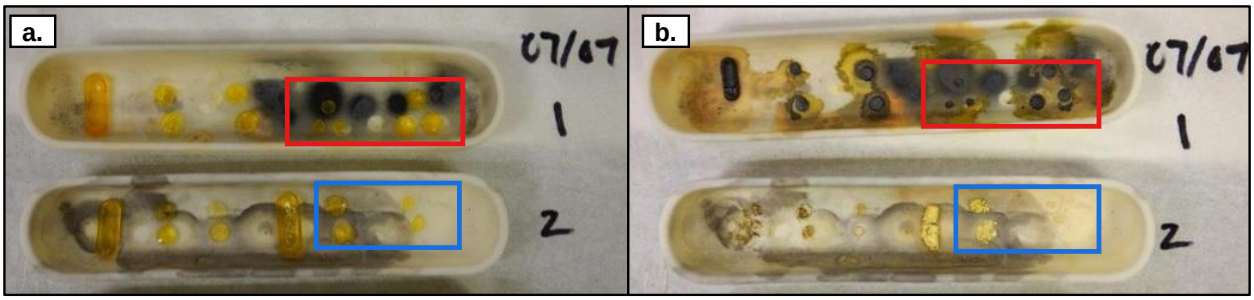

Figure S2. When infiltrated with UO_2^{2+} and Ce^{3+} cations, the dilute organogels shrink significantly in size prior to and after calcination. (a) in the red box is UO_2^{2+} infiltrated organogels, dilute on the left and concentrated on the right; the blue box is Ce^{3+} infiltrated organogels, dilute on the right and concentrated on the left. (b) post calcination, the ceramics are notably smaller than other conditions in the case of U (red box) and the only to remain intact in the case of Ce (blue box).

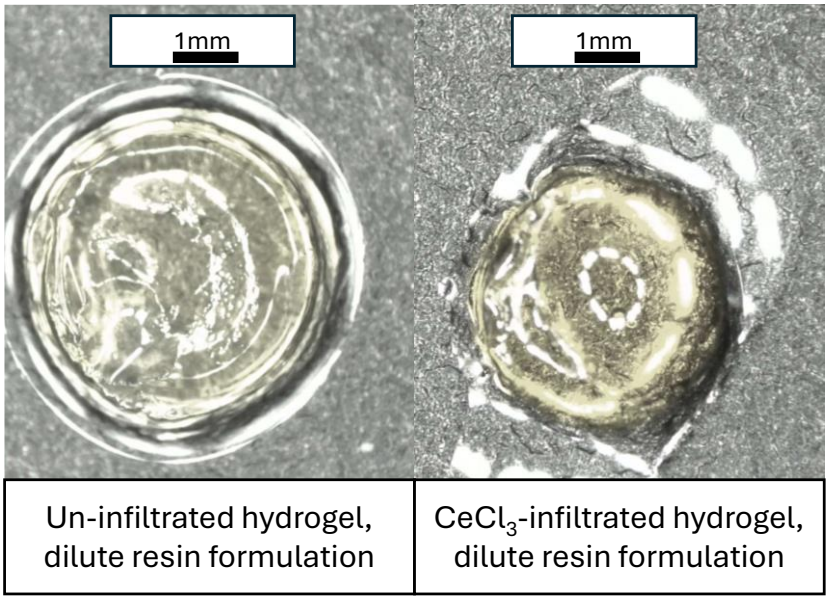

Figure S3. Microscope images taken at 1x zoom of plain hydrogel and $CeCl_3$ infiltrated hydrogels, both of dilute formulation. The infiltrated gel shrinks by approximately 0.9 mm in diameter after infiltration.

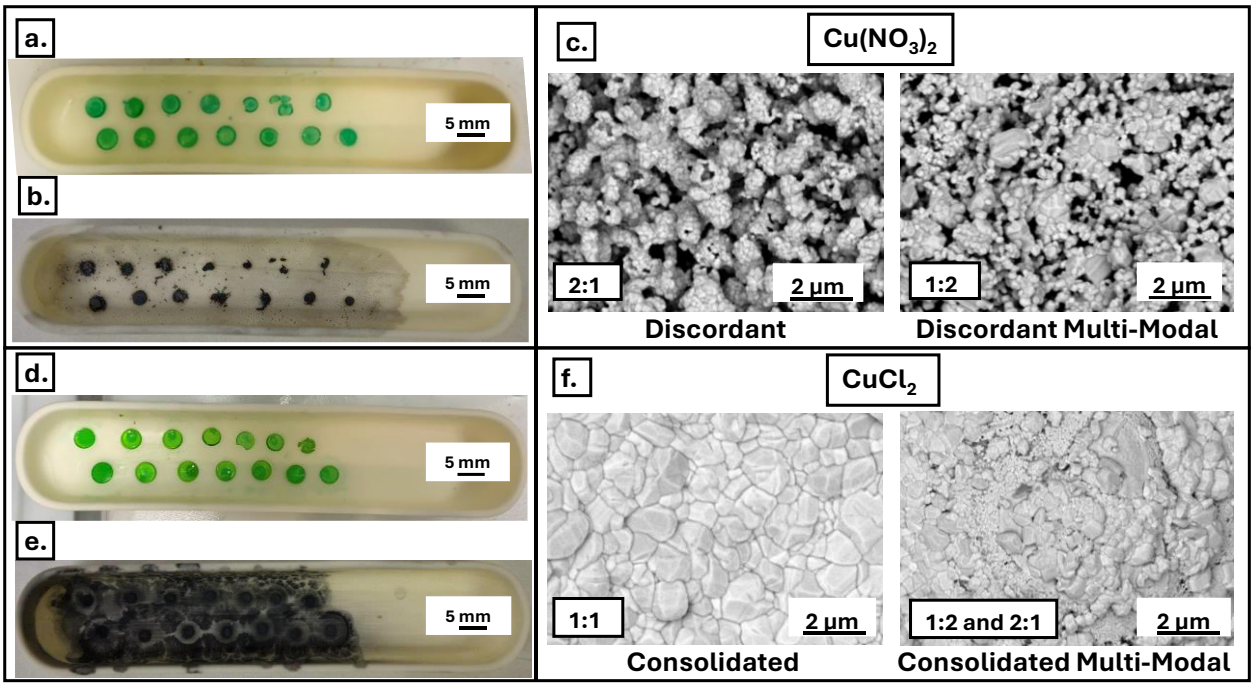

Figure S4. Impact of resin formulation and anion choice on CuO ceramics resulting from HIAM process. $Cu(NO_3)_2$ infiltration into gels left them light blue (a) and after calcination many were powdery and difficult to handle (b) SEM analysis showed that CuO from concentrated resin had a more porous, discordant microstructure when compared with those from diluted resin (c). $CuCl_2$ gave green hydrogels upon infiltration (d) and after calcination were easy to handle and solid (e); SEM analysis showed larger, consolidated grains for both concentrated and dilute resin conditions (f). The samples shown in the images on the left were exploratory samples of varying resin conditions, including 2:1 (far left) and 1:2 (far right). Samples were prepared in duplicate or triplicate and only intact samples were selected for analysis, when possible.

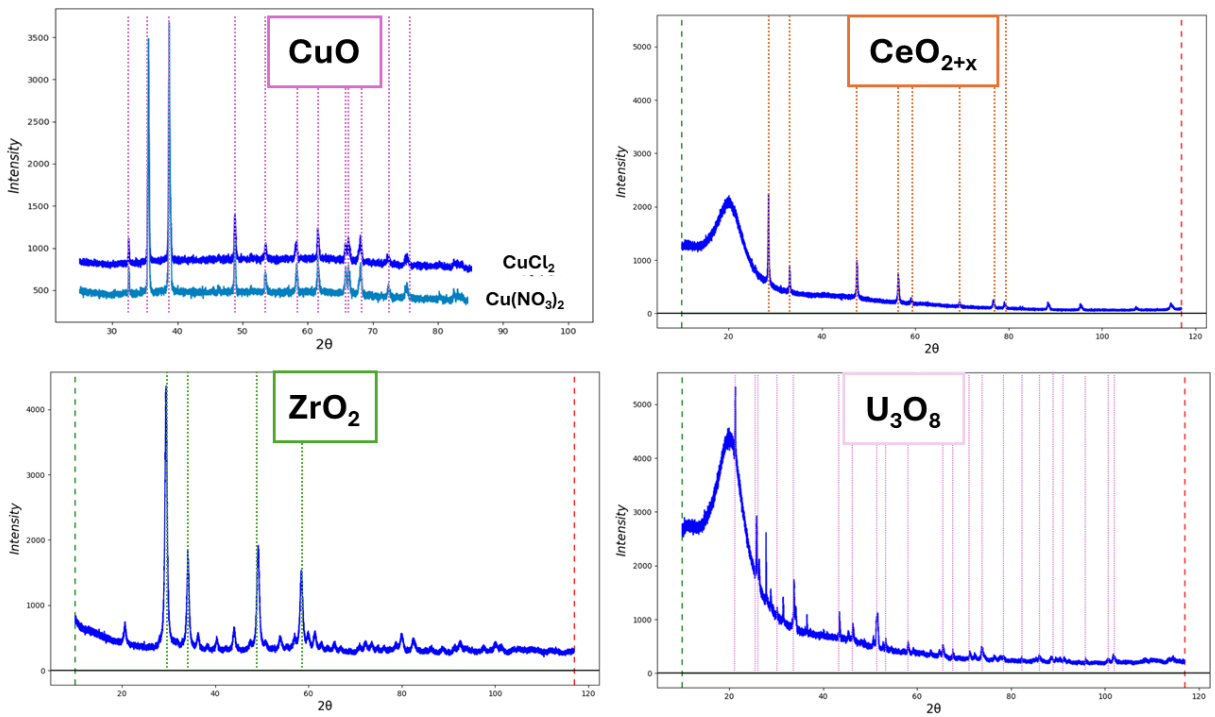

Figure S5. Powder X-ray Diffraction (XRD) data showing oxide phases resulting from the HIAM process, confirming oxide assemblage of varying purity. XRD data was collected with D8 Discover X-ray powder diffractometer (Bruker). Phases were matched using High Score Software, and visualized using GSAS-II.[1,2]

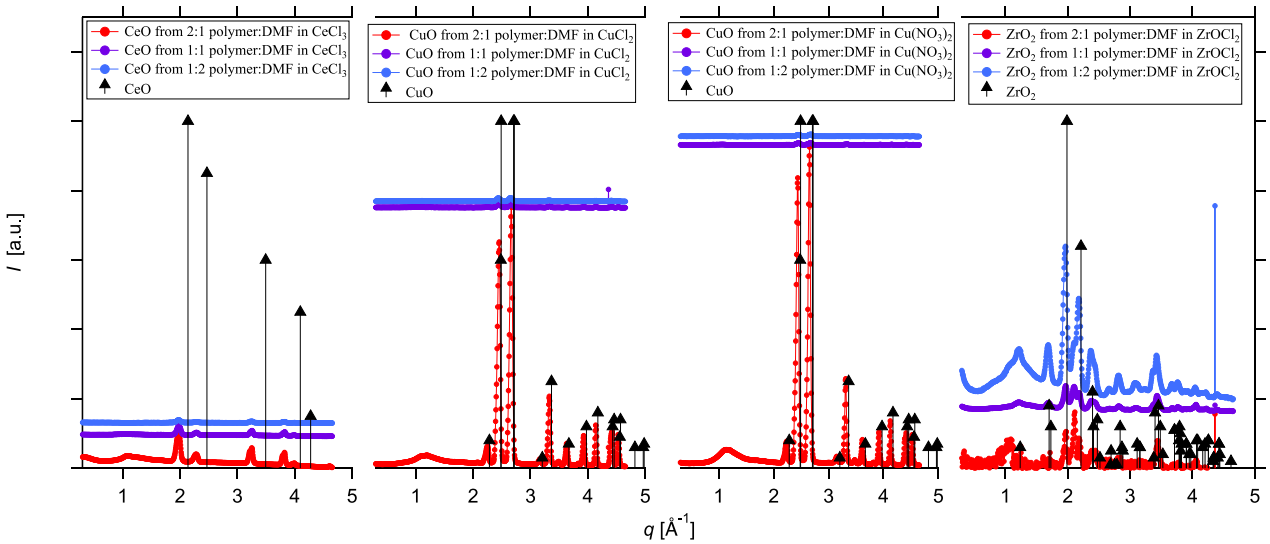

Figure S6. Small-angle X-ray scattering (SAXS) data showing oxide phases resulting from the HIAM process, confirming oxide assemblage of varying purity.

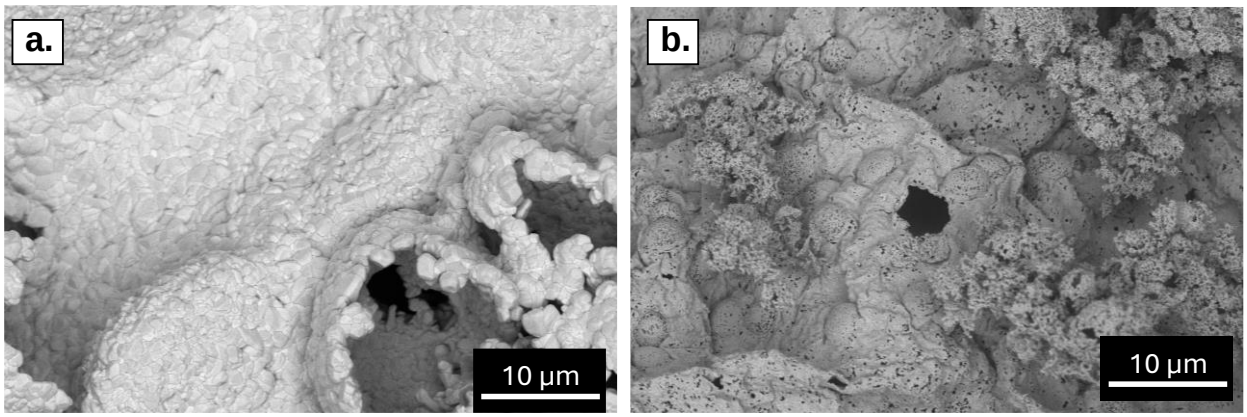

Figure S7. SEM images showing blister appearance in (a) $CuCl_2$ system (consolidated mode) and in (b) $Ce(NO_3)_3$ system (poorly consolidated mode).

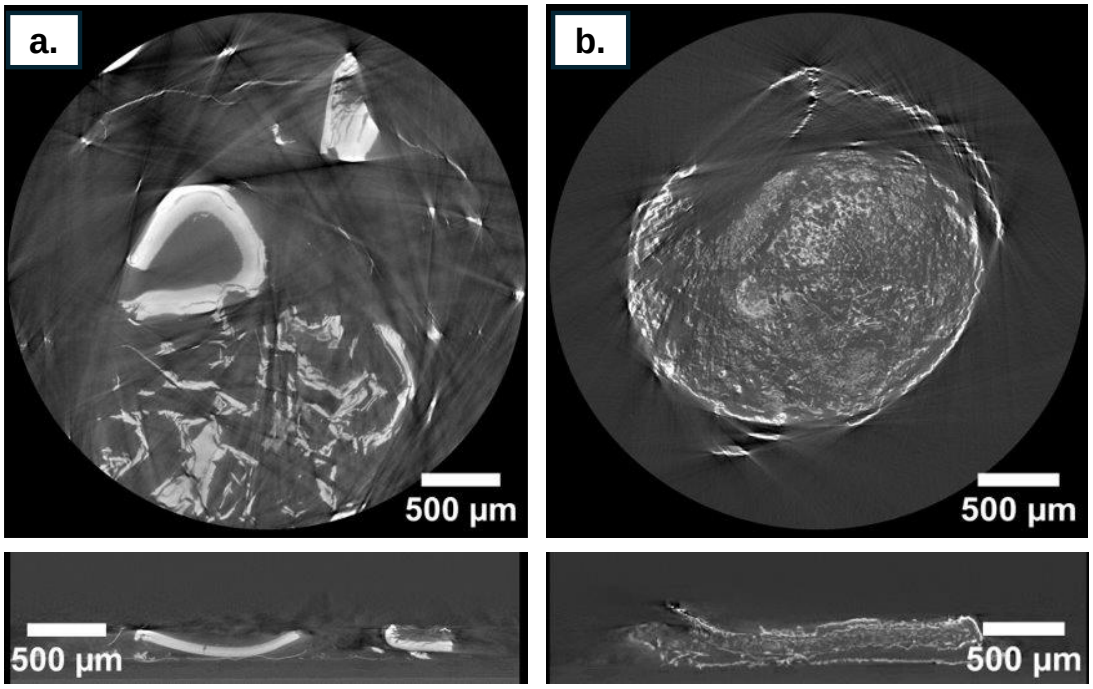

Figure S8. XCT reconstruction slices of ceramics resulting from (a) $Cu(NO_3)_2$ and (b) $CuCl_2$ infusion into hydrogels (1:1), along with their corresponding vertical cross-sections. Sample in a) has an approximate average thickness of 169 µm and sample in b) has an average thickness of 277 µm.

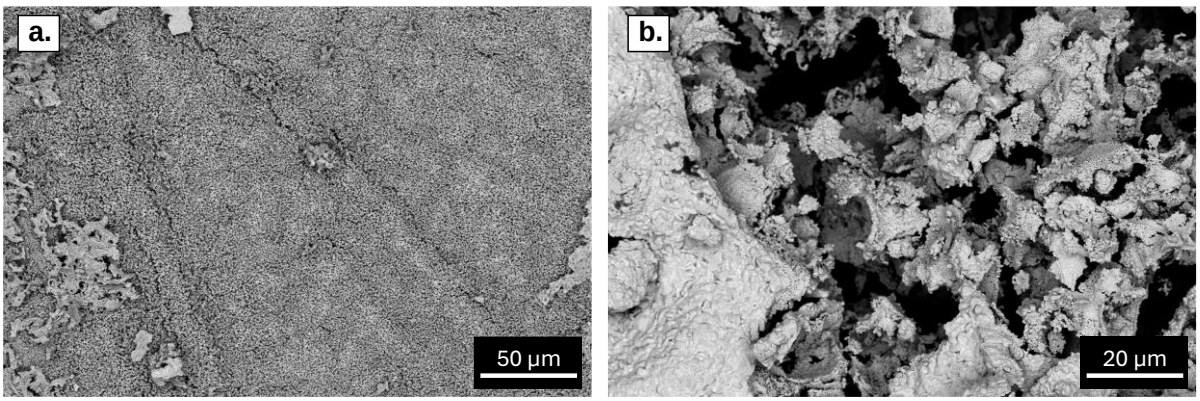

Figure S9. SEM of ceramics resulting from concentrated (2:1) hydrogel infused with (a) $Cu(NO_3)_2$ and (b) $CuCl_2$.

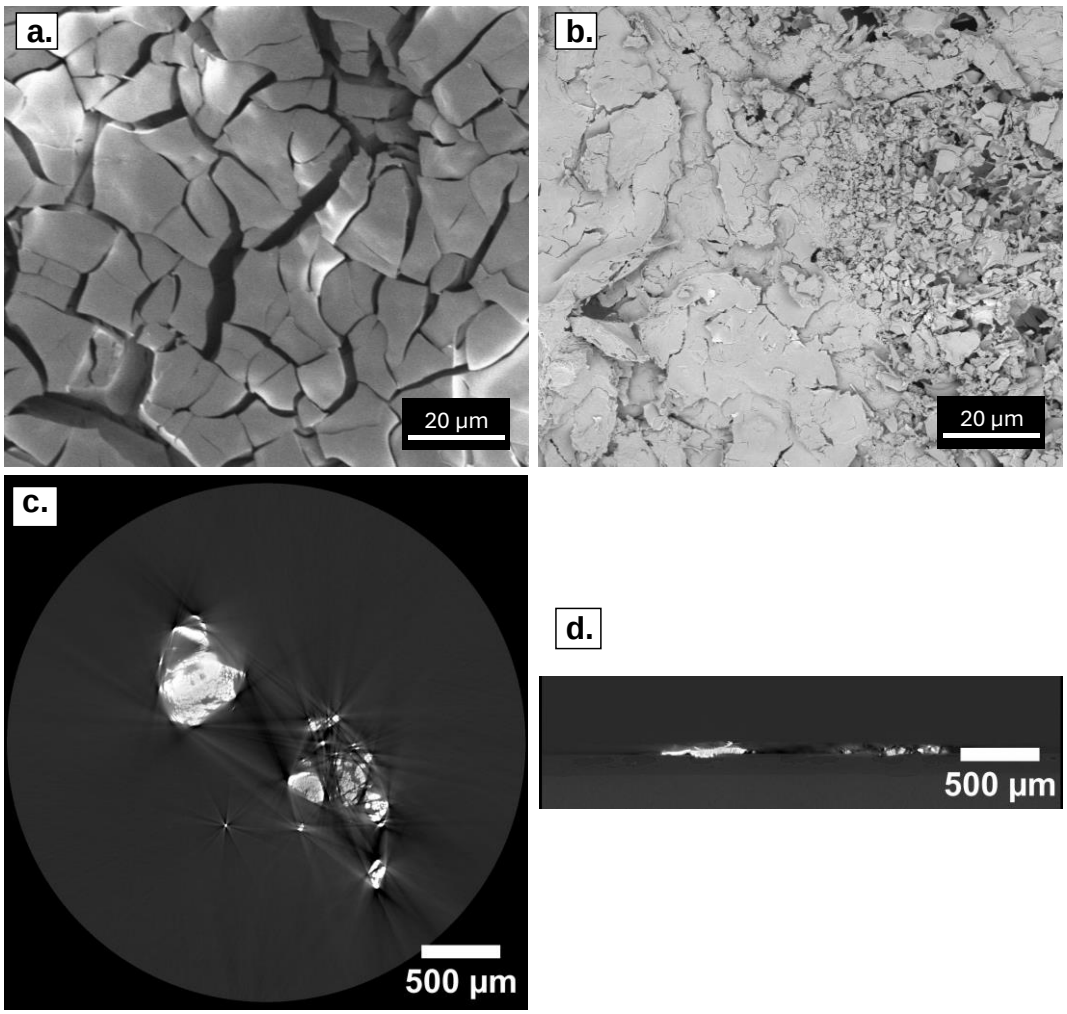

Figure S10. SEM of ceramics resulting from dilute (1:2) hydrogel infused with (a) $Ce(NO_3)_3$ and (b) $CeCl_3$. (c) XCT reconstruction slices of ceramics resulting from 2:1 infused $CeCl_3$ hydrogel, along with its corresponding vertical cross-section (d). Because this was only a piece of the resulting powder product, the average thickness of the sample was not determined.

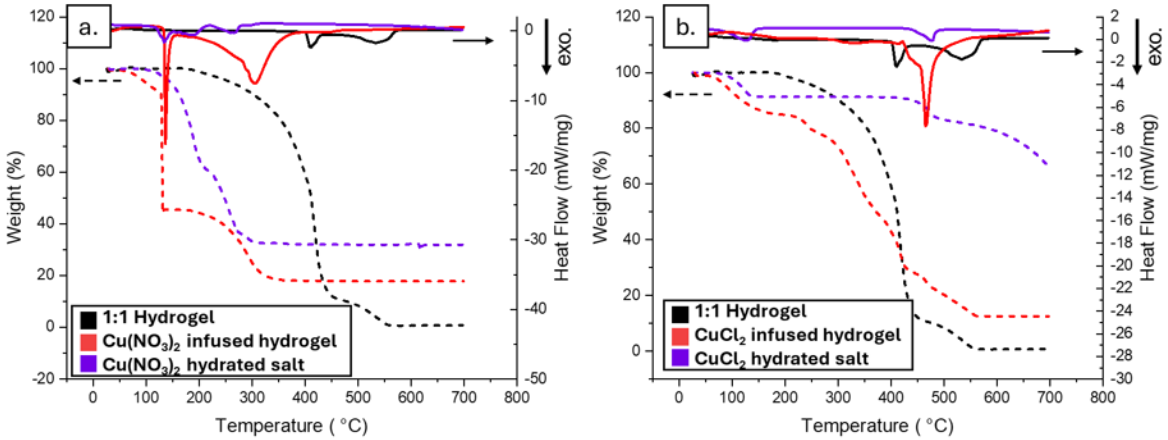

Figure S11. STA analysis of un-infiltrated 1:1 hydrogel (black), hydrogels infused with the copper salts (red), and hydrated copper salts (purple): (a) the nitrate system and (b) the chloride system. Evolution of temperature-dependent weigh % (TGA in dashed lines; left y-axis) and heat flow rate (DSC in solid lines; right y-axis) as a function of temperature up to 700 °C, with a heating ramp rate of 10 °C/min. Both nitrate and chloride infiltrated gels bear a closer resemblance to the hydrogels than the salts.

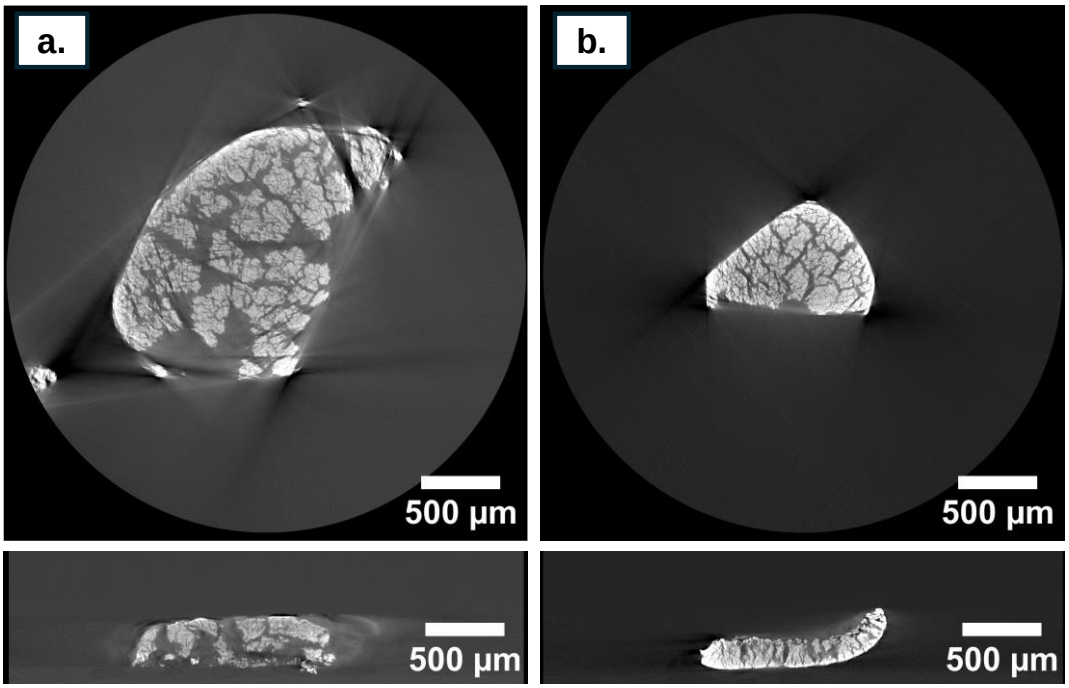

Figure S12. XCT reconstruction slices of ceramics resulting from $ZrOCl_2$ infusion into (a) concentrated hydrogel (2:1) and (b) hydrogel (1:1), along with their corresponding vertical cross-sections. Sample in a) has an average thickness of 320 µm and in b) average thickness is 177 µm.

Supplementary Tables

Table S1. Decomposition pathways of Ce salts.

Thermal decomposition of $Ce(NO_3)_3 \cdot 6H_2O$[3]	Thermal decomposition of $CeCl_3 \cdot 7H_2O$[4]
$Ce(NO_3)_3 \cdot 6H_2O \rightarrow Ce(NO_3) + 6H_2O$ $Ce(NO_3)_3 \rightarrow Ce(NO_3)_2 + NO_2 + ½\ O_2$ $Ce(NO_3)_2 \rightarrow CeNO_3 + NO_2 + ½\ O_2$ $CeNO_3 + ½\ O_2 \rightarrow CeO_2 + NO_2$	$CeCl_3 \cdot 7H_2O \rightarrow CeCl_3 + 7H_2O$ $CeCl_3 + 3\ H_2O \rightarrow Ce(OH)_3 + 3\ HCl$ $4Ce(OH)_3 + O_2 + 2H_2O \rightarrow 4Ce(OH)_4$ $Ce(OH)_4 \rightarrow CeO_2 + 2H_2O$ AND $2CeCl_3 + 2O_2 \rightarrow 2CeO_2 + 3Cl_2$

Table S2. Decomposition pathways of Zr oxo salts.

Thermal decomposition of $ZrO(NO_3)_2 \cdot 6H_2O$[5]	Thermal decomposition of $ZrOCl_2 \cdot 6H_2O$[5]
$ZrO(NO_3)_2 \cdot 6H_2O \rightarrow t\text{-}ZrO_2 + m\text{-}ZrO_2$ $t\text{-}ZrO_2 \rightarrow m\text{-}ZrO_2$	$ZrOCl_2 \cdot 6H_2O \rightarrow t\text{-}ZrO_2$ $t\text{-}ZrO_2 \rightarrow m\text{-}ZrO_2$

Table S3. Decomposition pathways of $UO_2(NO_3)_2$.

Thermal decomposition of $UO_2(NO_3)_2 \cdot 6H_2O$[4]
$UO_2(NO_3)_2 \cdot 6H_2O \rightarrow UO_2(NO_3)_2 \cdot 2H_2O + 4H_2O$ $UO_2(NO_3)_2 \cdot 2H_2O \rightarrow UO_2(OH)NO_3 + H_2O + HNO_3$- $UO_2(OH)NO_3 \rightarrow UO_3 + HNO_3$ AND $UO_2(NO_3)_2 \rightarrow UO_3 + 2NO_3 + ½\ O_2$ $3UO_3 \rightarrow U_3O_8 + ½\ O_2$

Supplementary References:

(1) Toby, B. H.; Von Dreele, R. B. GSAS-II: The Genesis of a Modern Open-Source All Purpose Crystallography Software Package. *J Appl Cryst* **2013**, *46* (2), 544–549. https://doi.org/10.1107/S0021889813003531.

(2) Degen, T.; Sadki, M.; Bron, E.; Konig, U.; Nenert, G. The HighScore Suite. *Powder Diffraction* **2014**, *29* (S2), S13–S18.

(3) Ayodele, B. V.; Hossain, M. A.; Chong, S. L.; Soh, J. C.; Abdullah, S.; Khan, M. R.; Cheng, C. K. Non-Isothermal Kinetics and Mechanistic Study of Thermal Decompoisiton of Light Rare Earth Metal Nitrate Hydrates Using Thermogravimetric Analysis. *Journal of Thermal Analysis and Calorimetry* **2016**, *125* (1), 423–235.

(4) Xue, S.; Wu, W.; Bian, X.; Wu, Y. Dehydration, Hydrolysis and Oxidation of Cerium Chloride Heptahydrate in Air Atmosphere. *Journal of Rare Earths* **2017**, *35* (11), 1156–1163. https://doi.org/10.1016/j.jre.2017.06.001.

(5) Štefanić, G.; Musić, S.; Popović, S.; Furić, K. Formation of ZrO_2 by the Thermal Decomposition of Zirconium Salts. *Croatica Chemica Acta* **1996**, *69* (1), 223–239.